

Use of streamflow indices to identify the catchment drivers of hydrograph

Jeenu Mathai¹ and Pradeep P. Mujumdar^{1,2}

¹Department of Civil Engineering, Indian Institute of Science, Bangalore, India

²Interdisciplinary Centre for Water Research, Indian Institute of Science, Bangalore, India

Correspondence to: Pradeep P. Mujumdar (pradeep@iisc.ac.in)

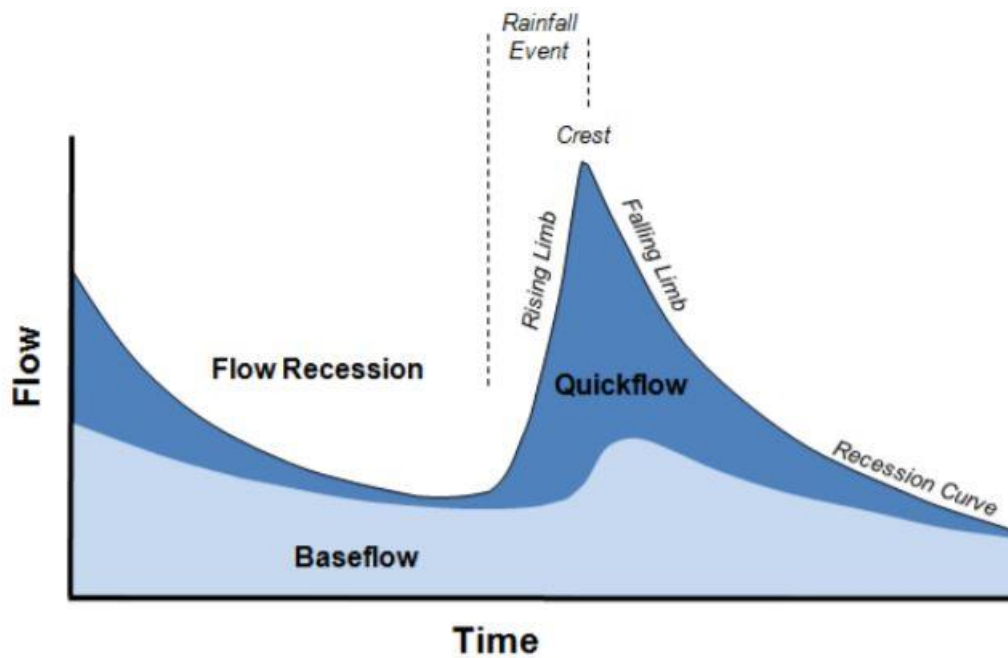
Abstract. Time irreversibility or temporal asymmetry refers to the steeper ascending and gradual descending parts of a streamflow hydrograph. The primary goal of this study is to bring out the distinction between streamflow indices directly linked with rising limbs and falling limbs and to explore their utility in uncovering processes associated with the steeper ascending and gradual descending limbs of the hydrograph within the time-irreversibility paradigm. Different streamflow indices are correlated with the rising and falling limbs and the catchment attributes. The key attributes governing rising and falling limbs are then identified. The contribution of the work is on differentiating hydrographs by their time irreversibility features and offering an alternative way to recognize primary drivers of streamflow hydrographs. A series of spatial maps describing the streamflow indices and their regional variability in the Contiguous United States (CONUS) is introduced here. These indices complement the catchment attributes provided earlier (Addor et al., 2017) for the CAMELS data set. Findings of the study revealed that the elevation, fraction of precipitation falling as snow and depth to bedrock mainly characterize the rising limb density, whereas the aridity and frequency of precipitation influence the rising limb scale parameter. Moreover, the rising limb shape parameter is primarily influenced by forest fraction, the fraction of precipitation falling as snow, mean slope, mean elevation, sand fraction, and precipitation frequency. It is noted that falling limb density is mainly governed by climate indices, mean elevation, and the fraction of precipitation falling as snow. However, the recession coefficients are controlled by mean elevation, mean slope, clay, the fraction of precipitation falling as snow, forest fraction, and sand fraction.

1 Introduction

Hydrologists use data to understand the hydrologic system by identifying several unique catchment signatures and employ various flow descriptors independent of statistical assumptions yet capable of capturing signals that reflect the basin's long-term unique behavior. Hydrological indices, commonly referred to as hydrologic metrics, hydrologic signatures, or diagnostic signatures, are quantitative flow metrics that characterize statistical or dynamical hydrological data series (McMillan, 2021). Specifically, streamflow indices are flow descriptors derived from discharge time-series data, and a considerable collection of indices are available to aid in the better characterization of hydrological features, ranging from basic statistics like the mean to more sophisticated metrics (Addor et al., 2018; McMillan, 2021). In many cases, daily streamflow records are not permitted for redistribution; however, researchers have computed streamflow indices and made them publicly accessible.

36 Hydrological indices are increasingly used in emerging areas such as global-scale hydrologic modeling and large-
37 sample hydrology to extract relevant information and compare the different watershed processes (Addor et al.,
38 2017, 2018; McMillan, 2021). These indices offer an indirect way to explore hydrological processes as well as
39 provide insights into hydrologic behavior in catchments where data other than streamflow is restricted and are
40 widely used in process exploration, model calibration, model selection, and catchment classification (Addor et al.,
41 2018; Clark et al., 2011; Kuentz et al., 2017; McMillan et al., 2011; Sawicz et al., 2011). McMillan (2021)
42 presented a classification that differentiates between statistics and dynamics-based signatures and between
43 signatures at different timescales.

44 The relevance of time irreversibility (or temporal asymmetry) of streamflow variability on a daily scale has been
45 emphasized in recent studies (Koutsoyiannis, 2020; Mathai and Mujumdar, 2019; Serinaldi and Kilsby, 2016).
46 The disparity in physical mechanisms driving the hydrograph's rising and falling limbs (Fig.1) contributes to time
47 irreversibility. Koutsoyiannis (2020) shows that irreversibility may be ignored at scales relevant to hydrological
48 applications in atmospheric processes, but it is critical to include irreversibility in studies related to streamflow.
49 Streamflow recessions convey valuable information about the basin storage properties and aquifer characteristics
50 (Aksoy & Bayazit, 2000). High variability encountered in the recession behaviour of individual segments is
51 always a challenge in modeling the recession limb (Tallaksen, 1995). Recessions do not follow a simple form due
52 to their nonlinear nature (Aksoy et al., 2001). Various segments of recession represent different stages in the flow
53 process and there is a need to differentiate the recession to various segments and to characterize the recession rates
54 separately. Such segmentation of recession curves enables us to reveal the nonlinear behavior of streamflow
55 dynamics. Time irreversibility must therefore be acknowledged in streamflow analysis, accounting for the
56 distinction of the recession into different segments, with a faster recession induced by high discharges caused by
57 surface runoff and a slower recession caused by baseflow (Fig.1), and the characterization of the recession rates
58 separately (Mathai and Mujumdar, 2019). In this study, streamflow indices are chosen to better understand
59 different hydrological processes by recognizing the streamflow hydrograph's temporal asymmetry. The novelty
60 in the work presented here is to differentiate hydrograph limbs by their time irreversibility property and use their
61 associated indices to provide an approach to derive insights on the primary drivers of streamflow hydrographs.



62 **Figure 1.** Schematic representation of rising limb and falling limb

63 (source: Environment Southland;

64 <https://www.es.govt.nz/environment/water/groundwater/groundwater-monitoring>)

65
66 The analysis employs a collection of indices drawn from hydrograph shape diagnoses, to extract information about
67 the properties of rising and falling limbs of the hydrograph. The principle of time irreversibility is encapsulated
68 by six streamflow indices that characterize the shape of a streamflow hydrograph.

69 The goals of this study are as follows: i) to identify the key drivers of streamflow hydrograph (rising and falling
70 limbs) in terms of catchment attributes (eg. mean slope, aridity, fraction of precipitation falling as snow) using
71 time-irreversibility-based indices; ii) to present a spatial map-based attribute class based on streamflow indices
72 for a large-sample hydrology dataset. The attribute class is a broad classification of attributes based on a particular
73 aspect/feature. *Topography, climate, and soil* are examples of attribute classes. In this study, we present a new
74 attribute class of streamflow indices related to rising and falling limbs, referred to as “*TI-streamflow indices*”
75 (*Time-irreversibility streamflow indices*).

76 Hydrograph analysis is referred to as the investigation of the numerous factors that influence hydrograph shape
77 (Rogers, 1972). The presence of hydrographs with a similar shape in long-term observation series of runoff
78 suggests that the same conditions of runoff generation reoccur from time to time in the catchment of a river due
79 to climate cyclicity and as a result of hydrological processes (Khrystyuk et al., 2017). Because climatic factors
80 are dynamic in space and time, they seem to be the most significant factors influencing the hydrograph shape
81 provided that changes in catchment conditions like land use are small. Khrystyuk et al., (2017) suggested that for
82 the Desna river basin in Russia, temperature, snow water equivalent, and snowmelt conditions are the most critical
83 factors influencing the shape of hydrographs. However, it is likely that these controls may not be equally important
84 controls on hydrograph across all regions globally. The shape, timing, and peak flow of a streamflow hydrograph
85 are influenced spatially and temporally by rainfall and watershed factors (Singh, 1997). One of the earlier studies
86 by Roberts and Klingeman (1970) investigated the influence of meteorological and physiographic parameters on
87 the runoff hydrograph using a physical laboratory model. Storm-related parameters (rainfall intensity, rainfall
88 duration, storm movement) and basin surface conditions are among the inputs that could be experimentally

89 modified in this model. The results revealed that each of these variables mentioned above has a substantial impact
90 on the hydrograph shape where certain factors had a more considerable effect on the rising limb of the runoff
91 hydrograph, whereas others were more important in terms of the flood crest (Roberts and Klingeman, 1970).

92 As shown in numerous studies in the literature, our notion of time-irreversibility and its indices could also helpful
93 in understanding the catchment drivers of streamflow hydrographs. This study presents an attribute class of
94 hydrograph shape descriptors with temporal asymmetry. The significance of large-sample hydrology datasets in
95 open hydrologic science and their potential to improve hydrological studies' transparency is also underlined in
96 this study.

97 Large-sample hydrology (LSH) gathers information from a large number of catchments to gain a more
98 comprehensive understanding of hydrological processes and to go beyond individual case studies. LSH helps
99 identify catchment behavior and leads one to derive precise conclusions regarding different hydrological
100 processes and models (Addor et al., 2020). Studies involving large-sample catchments help in understanding the
101 drivers of hydrological change (Blöschl et al., 2019), in assessing hydrological similarity and classification
102 (Berghuijs et al., 2014; K. A. Sawicz et al., 2014), in predictions in ungauged basins (Ehret et al., 2014), and in
103 analysing model and data uncertainty (Coxon et al., 2014) and foster hydrology research by standardizing and
104 automating the creation of large-sample hydrology datasets worldwide (Addor et al., 2020). LSH assists in
105 exploring interrelationships between numerous catchment attributes related to landscape, climate, and hydrology
106 (Addor et al., 2017; Alvarez-Garreton et al., 2018; Gupta et al., 2014; Newman et al., 2015; Sawicz et al., 2011)
107 and generalizing rules that can significantly improve the predictability of the water cycle (Alvarez-Garreton et al.,
108 2018).

109 The primary challenges in fostering LSH are data availability and accessibility, which seriously hinder its use in
110 data-scarce regions. Despite the fact that a few large-scale hydrology studies have been undertaken, the number
111 of publicly available large-scale datasets is still restricted (Addor et al., 2017, 2020; Coxon et al., 2020). Moreover,
112 licensing restrictions and strict access policies make the datasets rarely available to the public (Coxon et al., 2020).

113 Model Parameter Estimation Experiment project (MOPEX) dataset (Duan et al., 2006), Canadian model parameter
114 experiment (CANOPEX) database (Arsenault et al., 2016), Global Streamflow Indices and Metadata Archive (Do
115 et al., 2018; Gudmundsson et al., 2018), Global Runoff Reconstruction (Ghiggi et al., 2019), HydroATLAS (Linke
116 et al., 2019) and the Catchment Attributes and MEteorology for Large-Sample studies (CAMELS) (Addor et al.,
117 2017) are notable contributions of open and accessible large-sample catchment datasets (Coxon et al., 2020). The
118 concept of time irreversibility-based streamflow indices is then applied to CAMELS catchments with the goal of
119 encouraging large-sample hydrology studies. The primary contribution of this study is to establish the distinction
120 between signatures directly linked with rising limbs and falling limbs and their utility in uncovering processes
121 associated with the hydrograph's steeper ascending and gradual descending limbs.

122 **2 Methods**

123 To facilitate an understanding of various hydrological processes and streamflow hydrograph drivers, the study
124 employs streamflow indices considering the streamflow hydrograph's temporal asymmetry. The description of
125 indices used in this study are tabulated in Table 1. Streamflow indices linked to each limb of the streamflow
126 hydrograph within the time-irreversibility paradigm are distinguished since hydrographs have rising and falling

limbs. The following indices are considered in the rising limb category: 1) rising limb density, 2) rising limb shape parameter, and 3) rising limb scale parameter. In contrast, 1) falling limb density 2) slope of upper recession (upper recession coefficient) 3) slope of lower recession (lower recession coefficient) are selected in falling limb category. The next step is to compute these indices for a large number of catchments and correlate them with attributes such as climate, topography, vegetation, geology, and soil. The streamflow indices can be correlated explicitly since sub-categories are involved in each of the catchment attributes discussed above. Finally, the key attributes governing rising and falling limbs can be summarized and identified. The specifics of indices are explained further below.

Rising limb density (RLD) is defined as the ratio of the number of rising limbs and the cumulative time of rising limbs (Shamir et al., 2005). RLD is a hydrograph shape descriptor without considering the flow magnitude (Fig. 2) and the expression for RLD is given as,

$$RLD = \frac{N_{RL}}{T_R} \quad (1)$$

The ratio of the number of falling limbs to the cumulative time of falling limbs is termed as falling limb density (FLD) (Fig. 2) (Shamir et al., 2005). The expression for FLD is given as,

$$FLD = \frac{N_{FL}}{T_F} \quad (2)$$

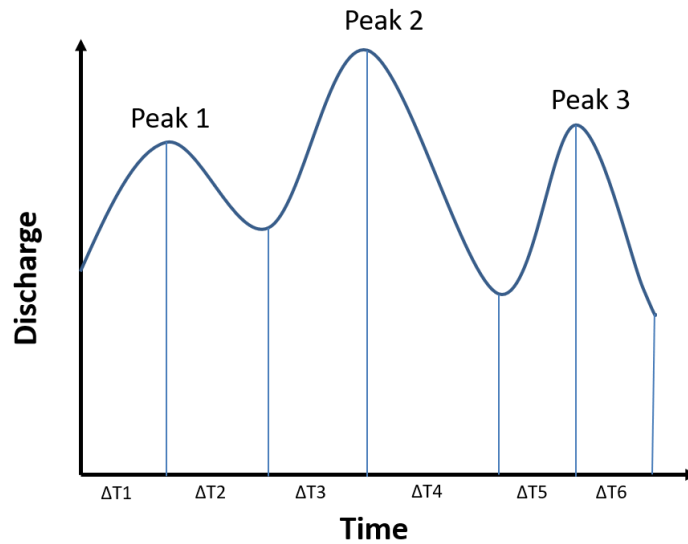
Table 1. Hydrological descriptors with temporal asymmetry.

Attribute		Description	Unit	Data source	References
Rising limb	RLD	Rising limb density	day ⁻¹	N15 – USGS data* (https://doi.org/10.5065/D6MW2F4D)	Shamir et al. (2005)
	a	Rising limb scale parameter	-		Mathai and Mujumdar, (2019)
	b	Rising limb shape parameter	-		Mathai and Mujumdar, (2019)
Falling limb	FLD	Falling limb density	day ⁻¹		Shamir et al. (2005)
	b ₁	Upper recession coefficient	-		Mathai and Mujumdar, (2019)
	b ₂	Lower recession coefficient	-		Mathai and Mujumdar, (2019)

* N15 covers 671 catchments in the contiguous USA (CONUS), which provides daily meteorological forcing and daily streamflow measurements from the United States Geological Survey (USGS).

$$\text{Rising limb density} = \frac{3}{\Delta T1 + \Delta T3 + \Delta T5}$$

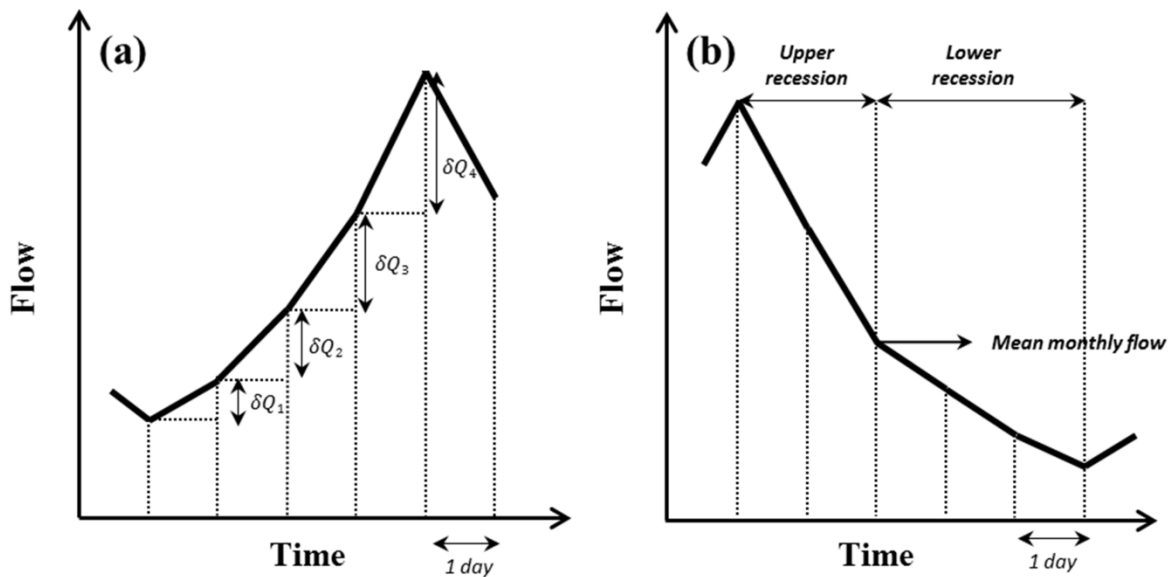
$$\text{Falling limb density} = \frac{3}{\Delta T2 + \Delta T4 + \Delta T6}$$



145

146 **Figure 2.** Schematic example of rising limb density (RLD) and falling limb density (FLD) calculation (Shamir et
 147 al., 2005).

148 We first identify the hydrologic state of the stream (ascension and recession) (Mathai and Mujumdar, 2019). To
 149 determine the hydrologic state of a stream - increasing (wet) or decreasing (dry) - on a given day, a time series of
 150 diurnal increments is extracted by differencing the original time series with its one-day lagged time series. The
 151 positive increments are identified as diurnal increments for wet days (ascension limb).



152

153 **Figure 3.** Schematic representation of flow series (a) ascension limb and (b) recession limb (Mathai and
 154 Mujumdar, 2019).

155 To characterize the shape of the rising limbs occurring on wet days, the diurnal increments are fitted using an
 156 appropriate probability density function. The Weibull distribution reflects the diurnal increments of streamflow
 157 that occur on wet days satisfactorily (Mathai and Mujumdar, 2019; Stagge and Moglen, 2013; Szilagyi et al.,
 158 2006), and the scale 'a' and shape 'b' parameters of the Weibull distribution are computed for each catchment by
 159 using observed diurnal increments of streamflow (indicating δQ) of the ascension limb (Fig 3.a). The Weibull pdf
 160 is positive only for positive values of x , and is zero otherwise. For strictly positive values of the scale parameter
 161 a and shape parameter b , the density function is given by

$$f(x; a, b) = \begin{cases} \frac{b}{a} \left(\frac{x}{a}\right)^{b-1} e^{-(x/a)^b} & x \geq 0, \\ 0 & x < 0, \end{cases} \quad (3)$$

162 where $a > 0$, $b > 0$. The shape and scale parameters of the Weibull distribution are estimated for each catchment
 163 from the observed diurnal increments of the streamflow. The scale parameter controls the magnitude of the
 164 increasing limb, whilst the shape parameter reflects the flashiness of the increasing limb. The scale parameter is
 165 related to the magnitude of storm events which mirrors the general shape of flows in the stream. As a result,
 166 correlating these parameters with catchment attributes reveals which catchment attributes drive the magnitude and
 167 flashiness of rising limbs.

168 In contrast, an exponential recession is used to capture the shape of the falling limbs on dry days of the daily
 169 hydrograph, representing the falling limbs' underlying dynamics (Mathai and Mujumdar, 2019). As the upper
 170 recession refers to the fast flow following a storm event and the lower recession refers to the baseflow recession,
 171 falling limb modeling is done in two stages (Fig 3.b) (Aksoy, 2003; Aksoy and Bayazit, 2000). The steps to obtain
 172 recession coefficients b_1 and b_2 are explained below (Mathai and Mujumdar, 2019). To portray the shape of the
 173 recession limbs occurring on dry days of the daily hydrograph, an exponential recession is employed to capture
 174 the falling limbs' underlying dynamics (Mathai & Mujumdar, 2019). The expression for the exponential recession
 175 is given as follows,

$$Q_t = Q_0 e^{-bt} \quad (4)$$

176 where b is the recession coefficient, t is time, Q_t is the flow t days after the peak and Q_0 is the peak flow (Mathai
 177 & Mujumdar, 2019). Mean flow value is chosen as an appropriate measure (Sargent, 1979) to divide the recession
 178 into two stages. The limbs with a peak flow value greater than the observed mean flow value are considered as
 179 upper recessions and those with peak flow values smaller than the observed mean as lower recessions. However,
 180 it may be noted that using the mean monthly flow can lead to unusual situations if peak flow for a given event is
 181 below the monthly mean. In such cases, the entire recession would be classified as a lower recession curve, and
 182 no upper part would exist. In those situations, there are still different driving processes for the first and second
 183 part of the recession, but these would all be lumped into one category in this case. Since we are dealing with the
 184 long-term time series, the recession slope will be nearly constant for a catchment and does not vary much with
 185 the recession separation technique used. In this study, we calculate recession slope at an annual scale. The upper
 186 recession is modelled as follows,

$$Q_t = Q_0 e^{-b_1 t} \quad (5)$$

187 where b_1 is the recession coefficient for the upper part of the recession limb, t is the number of days after the
188 peak, Q_t is flow t days after the peak, Q_0 is the preceding peak flow (Mathai & Mujumdar, 2019). The lower
189 recession is represented as,

$$Q_t = Q_0^* e^{-b_2(t-t^*)} \quad (6)$$

190 where b_2 is the recession coefficient for the lower part of the recession limb, t^* is the time from the start of the
191 lower recession, Q_0^* is the initial flow in the lower part of the recession (Mathai & Mujumdar, 2019). The recession
192 expressions for upper and lower recession are fitted by regressing $\ln(Q_t/Q_0)$ versus t and $\ln(Q_t/Q_0^*)$ versus $t -$
193 t^* respectively. These linear regressions are performed on each individual recession sequence. The average of the
194 upper/lower recession parameters is taken as the upper/lower recession parameter of that catchment (on daily time
195 series data).

196 The study uses indices related to rising limb (viz., RLD, rising limb scale parameter, rising limb shape parameter)
197 and recession limb (viz., FLD, upper recession coefficient, lower recession coefficient) to summarize the
198 characteristic shape of steeper rising and gradually declining falling limb and its application in understanding the
199 role of various drivers of catchment attributes in streamflow generation.

200 **3 Dataset used**

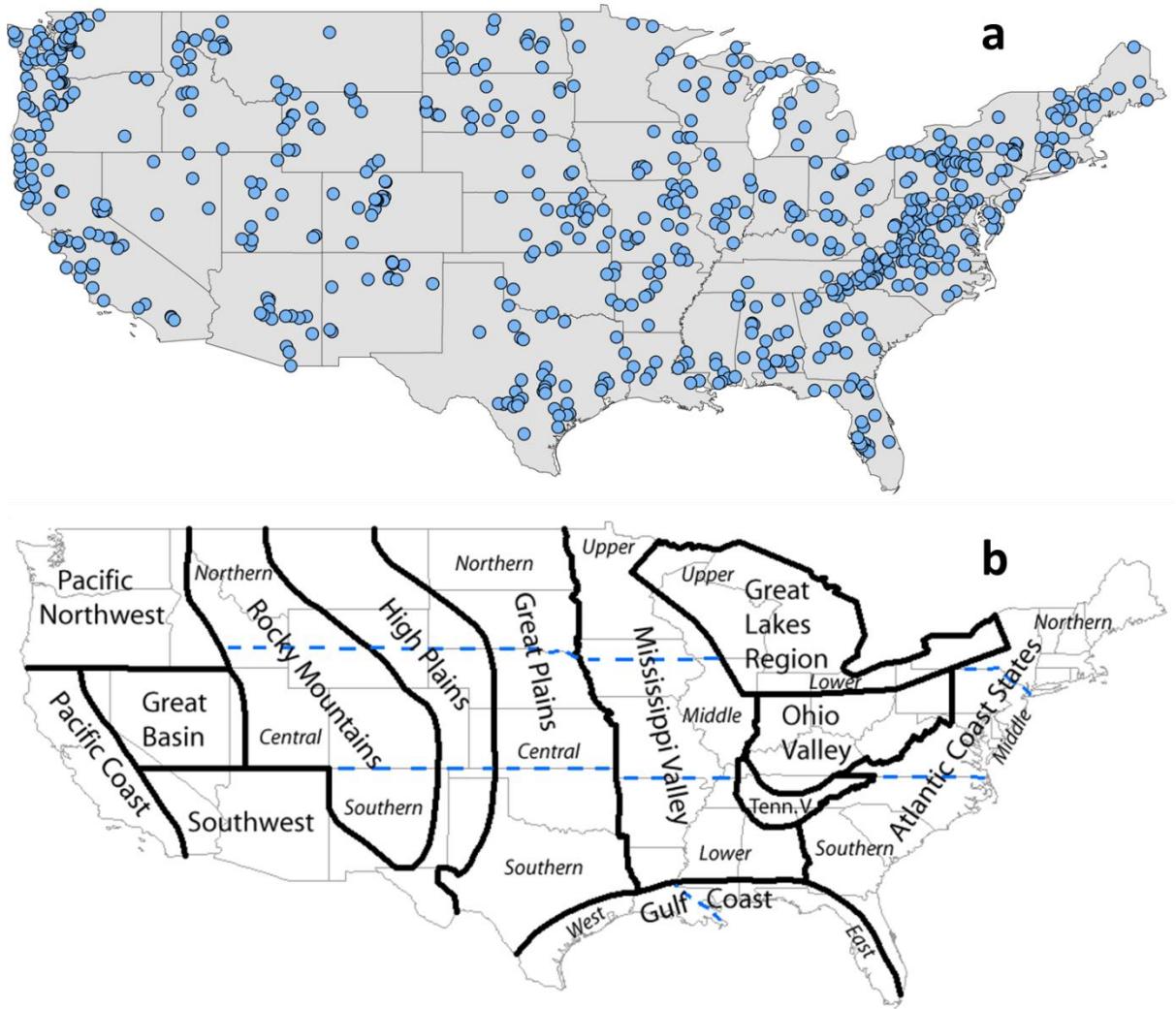
201 Section 3 provides the description of the dataset used and the study area chosen. This study employs the CAMELS
202 dataset, which encompasses daily discharge data and catchment attributes for 671 catchments (Fig. 4) across the
203 continental United States, representing a diverse set of catchments with long streamflow time series covering a
204 wide range of hydro-climatic conditions (Addor et al., 2017). The time frame chosen for the analysis is from 1
205 October 1989 to 30 September 2009 (Addor et al., 2017).

206 The topographic characteristics of CAMELS dataset are represented in Fig. S1. Except for the Appalachian
207 Mountains, the eastern part of the Continental United States is much flatter than the western portion, according to
208 mean elevation and mean slope maps (Fig. S1.a and S1.b). Figure S1.c depicts the spatial pattern of catchment
209 size, highlighting presence of some catchments with an area greater than 10,000 km². The landscape of each
210 catchment is described using multiple attributes, which can be divided into various classes as shown in Table S1
211 (Addor et al., 2017).

212

213

214



215

216 **Figure 4.** (a) Map of 671 CAMELS catchments in the continental United States considered in this study. (b)
 217 Geographical regions of US according to NOAA National Centers for Environmental Information referred for the
 218 analysis (source: NOAA National Centers for Environmental Information; <https://www.ncdc.noaa.gov/temp-and-precip/drought/nadm/geography>).
 219

220

221 **4 Results and Discussion**

222 The regional variability of the streamflow indices is investigated by computing the rising limb density, falling
 223 limb density, rising limb scale parameter, rising limb shape parameter, upper recession coefficient, and lower
 224 recession coefficient for 671 CAMELS catchments and given as spatial maps. Streamflow indices are then
 225 presented in hydrological clusters to incorporate a more explicit spatial representation of catchment behavior
 226 across the CONUS. Catchment attributes cover a broad range of aspects of catchment hydrology such as: land
 227 cover, soil, climate, geology, topography and the association between these attributes and streamflow indices is
 228 discussed further in the subsequent section. It is important to understand the influence of climatic zones on the
 229 streamflow indices, as climate attributes influence the catchment streamflow dynamics (Addor et al., 2018;
 230 Berghuijs et al., 2014; Jehn et al., 2020; Knoben et al., 2018; Stein et al., 2021). Since the catchments are
 231 distributed in varied climatic zones (Jehn et al., 2020; Knoben et al., 2018; Stein et al., 2021), the CAMELS data

232 is ideal for addressing this question. With this motivation, the effect of climate attributes on streamflow indices
233 associated with rising and falling limbs is investigated here.

234 **4.1 Spatial Variability in Streamflow Indices and Relation of the Streamflow Indices with Catchment** 235 **Attributes**

236 Streamflow indices related to rising limbs and falling limbs are computed for the selected catchments and
237 displayed in spatial maps as shown in Fig. 5 and Fig. 6, respectively. The spatial analysis is based on the United
238 States' geographical areas (for details, refer to Fig. 4b) as defined by NOAA's National Centers for Environmental
239 Information and is referred to in the following spatial maps. Furthermore, the clusters provided by Jehn et al.
240 (2020) to represent the discrete hydrological behaviors of the continental United States are adopted in this study
241 to understand the regional variability of catchment behavior. Figure S2 and Table S2 present the location map and
242 details of the ten clusters. Figure S3 shows Boxplots of the catchment attributes of the clusters (after Jehn et al.,
243 2020).

244 Even though a comprehensive dataset such as CAMELS provides an excellent overview of various catchments in
245 contrasting climatic and topographic regions, it does not by itself provide insights to explain hydrologic behavior.
246 We present here streamflow indices in clusters representing distinct hydrological behavior, enabling an
247 understanding of the hydrological processes. Jehn et al. (2020) summarize the characteristics of each catchment
248 cluster in terms of climate, hydrology and location. The clusters presented by Jehn et al. (2020) are formed based
249 on agglomerative hierarchical clustering with ward linkage on the principal components of the hydrological
250 signatures. The hydrological signatures identified with the highest spatial predictability are used to cluster 643
251 catchments from the CAMELS dataset (Jehn et al., 2020). This facilitates straightforward interpretations of the
252 observations to explain the hydrologic behavior in each cluster.

253 In this paper, we first identify the regions in the United States where high/low values of streamflow indices occur.
254 The dominant catchment attributes of these regions are also identified using corresponding clusters. The
255 streamflow indices and the dominant catchment attribute are then related to interpreting the obtained findings'
256 process. In terms of geographical regions, the rising limb density is highest over the Atlantic coast states, Ohio
257 valley, Lower Mississippi Valley, Southern Great Plains, Southwest and Pacific, and lowest along the Upper Great
258 Lakes region, Upper Mississippi Valley, Great Basin, and Northern Rocky Mountains, Northern Interior Plains,
259 and East of Gulf Coast (Fig. 5.a). Further, in terms of hydrological clusters, the Appalachian Mountains (Cluster
260 10), Southeastern and Central Plains (Cluster 1), and all Southern most states of the US (Cluster 9) witness high
261 rising limb densities (Fig. 6.a). Cluster 1 is characterized by dense vegetation cover and low elevation resulting in
262 little annual snowfall. Cluster 10 catchments are located in the Appalachian Mountains, with a higher mean
263 elevation than most other clusters, experiencing low aridity and high forest cover. However, Cluster 9
264 encompasses all of the United States' southern states, with lower precipitation seasonality and higher forest cover
265 and green vegetation. Furthermore, all of the catchments in Cluster 9 are very near the sea, with a low snow
266 component and high evapotranspiration. We used Spearman rank correlation for the correlation analysis (Table
267 2). Green-colored coefficients represent positive correlation, and the red-colored correlation coefficients represent
268 negative correlation (Table 2). It can be seen that the rising limb density shows a negative correlation (Table 2)
269 with the area ($r = -0.30$), elevation ($r = -0.20$) fraction of precipitation falling as snow ($r = -0.33$), and depth to
270 bedrock ($r = -0.32$). Northwestern Forested Mountains (Clusters 3, 4), located in the mountains of the western US,

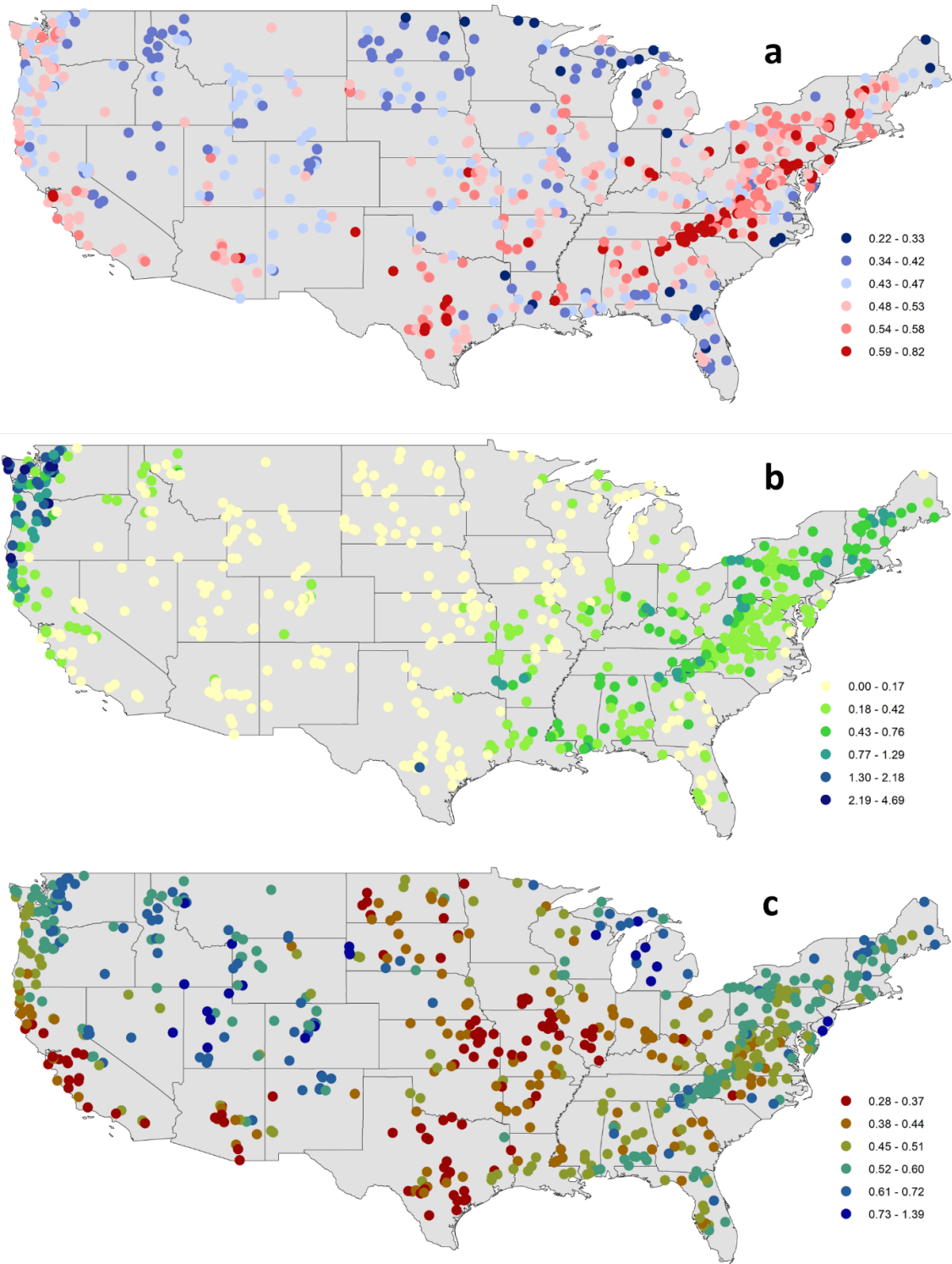
271 experience low values of rising limb density. The catchments of Cluster 3 have the largest snow storage in the
272 dataset. Cluster 4 is found in the western United States' mountains, where there is a lot of snow, same as Cluster
273 3. Low values of rising limb density are observed due to a negative correlation with the fraction of precipitation
274 falling as snow ($r = -0.33$). The study indicates that rising limb density is mainly governed by elevation and
275 fraction of precipitation falling as snow in the CONUS.

276 Considerably low values of rising limb scale parameters are experienced over the Rocky Mountains, High Plains,
277 Great Plains, Upper Mississippi Valley, Great Basin, Southwest, and the Great Lakes regions, whereas the Pacific
278 Northwest shows high values of rising limb scale parameters (Fig. 5.b). Clusters (5, 7) over the Northwestern
279 Forested Mountains of CONUS experience very high values of rising limb scale parameters (Fig. 6.b). These
280 catchments have the highest discharge, especially in the early summer, due to a combination of high precipitation
281 and snowmelt. Further, the region in the Continental US which receives the highest precipitation is included in
282 Cluster 5. Moreover, Cluster 5 consists of a large proportion of forest. Again, Cluster 7 with high values of rising
283 limb scale parameter is characterized by high fraction of precipitation falling as snow. High precipitation and
284 snowmelt might result in a large discharge. Higher discharges can create higher values of rising scale parameters
285 as the rising limb scale parameter regulates the magnitude of the rising limb. Low values of rising limb scale
286 parameters are shown by Clusters 2, 8, 9. This is because of low water availability, low snow fraction precipitation
287 falling as snow, and high evaporation experienced in these regions. Low discharge and thus lower rising limb
288 scale parameters can be caused by excessive evaporation, low water availability, and a low snow fraction of
289 precipitation falling as snow. It is observed that the rising limb scale parameter (Table 2) shows a negative
290 correlation with climate ($r = -0.53$ for aridity) and a positive association with the vegetation attributes ($r = 0.46$
291 for forest fraction, $r = 0.41$ for LAI maximum, $r = 0.44$ for green vegetation fraction maximum). Frequency of
292 precipitation ($r = -0.56$ for high precipitation frequency, $r = -0.63$ for low precipitation frequency) display a strong
293 negative association with the rising limb scale parameter.

294 Low rising limb shape parameter occurs along the Great Plains, Mississippi Valley, Pacific coast, and the west of
295 Gulf Coast (Fig. 5.c). In contrast, the shape parameter over the Rocky Mountains, High Plains, Great Basin, Pacific
296 Northwest, and the Great Lakes region witnesses the highest values of rising limb shape parameters (Fig. 5.c). All
297 the catchments located in the Southern states of the US (Cluster 9), Great Plains and North American deserts
298 (Cluster 8), and the Central Plains (Cluster 2) characterize low values of rising limb shape parameters (Fig. 6.c).
299 This is due to low water availability, low snow fraction precipitation falling as snow, low leaf area index, and high
300 evaporation experienced in these regions. Excessive evaporation and a low snow fraction of precipitation falling
301 as snow can contribute to low discharge and thus lower rising limb shape parameters. It is noted that the rising
302 limb shape parameter indicates (Table 2) a positive correlation with vegetation attributes ($r = 0.41$ for forest
303 fraction) and the fraction of precipitation falling as snow ($r = 0.53$), mean slope ($r = 0.36$), mean elevation ($r =$
304 0.41), and sand fraction ($r = 0.37$) whereas, it negatively correlates with precipitation frequency ($r = -0.42$ for high
305 precipitation frequency and $r = -0.45$ for low precipitation frequency). High values of rising limb shape parameters
306 are seen in Clusters 3, 4 (Fig. 6.c) located in the Northwestern Forested Mountains of the western US, dominant
307 with a summer peak of discharge caused by rapid snowmelt. The rapid snowmelt can cause flashy hydrographs
308 with high values of rising limb shape parameters.

309 Catchments with a high falling limb density are predominantly located along the Great Basin and the Rocky
310 Mountains and in the High Plains region (Fig. 7.a). This is due to less forest cover in these arid regions and falling
311 limb density shows a positive association with the arid climate ($r = 0.39$). Clusters 6, 7 over Marine West Coast
312 Forests and Western Cordillera experience smaller falling limb densities (Fig. 8.a). We can see that falling limb
313 density is mainly governed by climate indices and is negatively correlated with the land cover characteristics (for
314 LAI maximum ($r = -0.37$) and green veg frac max ($r = -0.40$, Table 2). Mean elevation ($r = 0.55$) also strongly
315 characterizes the nature of the falling limb density. Besides, fraction of precipitation falling as snow ($r = 0.42$) is
316 also positively correlated with falling limb density.

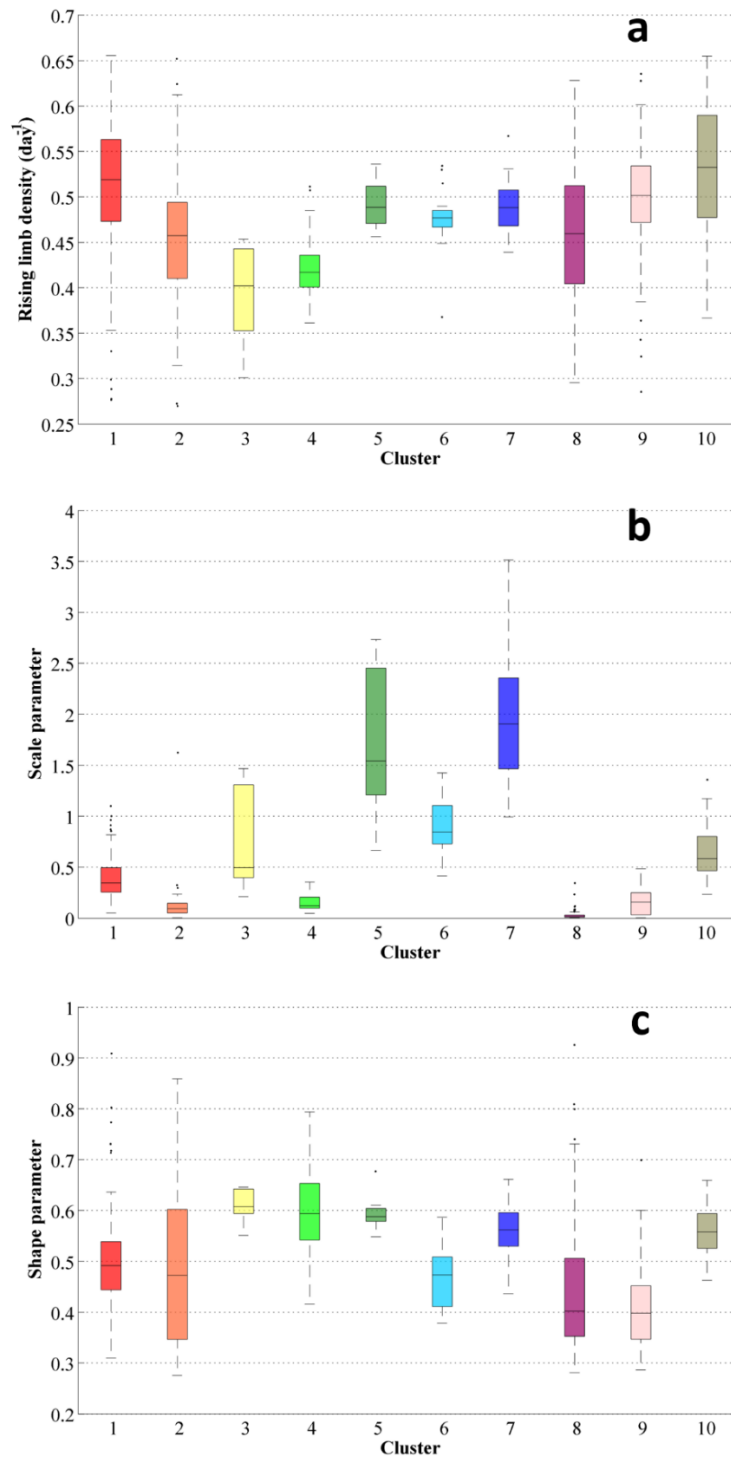
317 Similarities exist between the patterns of the upper recession coefficient and the lower recession coefficient (Fig.
318 7.b and Fig. 7.c). Clusters 3, 4 located in the Northwestern Forested Mountains, which have overall low discharge,
319 show low values of upper and lower recession coefficients (Fig. 8.b and Fig. 8.c). Clusters 2 and 9, located in the
320 eastern US, witness high values of recession coefficients; due to low slope inclinations, water takes a long time
321 to reach the outlet (Fig. 8.b and Fig. 8.c). Recession coefficients are negatively correlated (Table 2) with
322 topographic indices (with mean elevation: upper_r = -0.40, lower_r = -0.35; with mean slope: upper_r = -0.38,
323 lower_r = -0.37, where upper_r and lower_r corresponds to correlation values of upper and lower recession
324 coefficients respectively). Further, the recession coefficients show a positive correlation with clay (upper_r = 0.52,
325 lower_r = 0.32) and negative correlations with the fraction of precipitation falling as snow (upper_r = -0.46,
326 lower_r = -0.39), forest fraction (upper_r = -0.31, lower_r = -0.28), and sand fraction (upper_r = -0.38, lower_r =
327 -0.23). Moreover, the geology attributes such as subsurface porosity (upper_r = 0.13, lower_r = 0.16) reveal a
328 positive correlation to recession coefficients and a negative (upper_r = -0.09, lower_r = -0.18) with subsurface
329 permeability (Table 2).



330

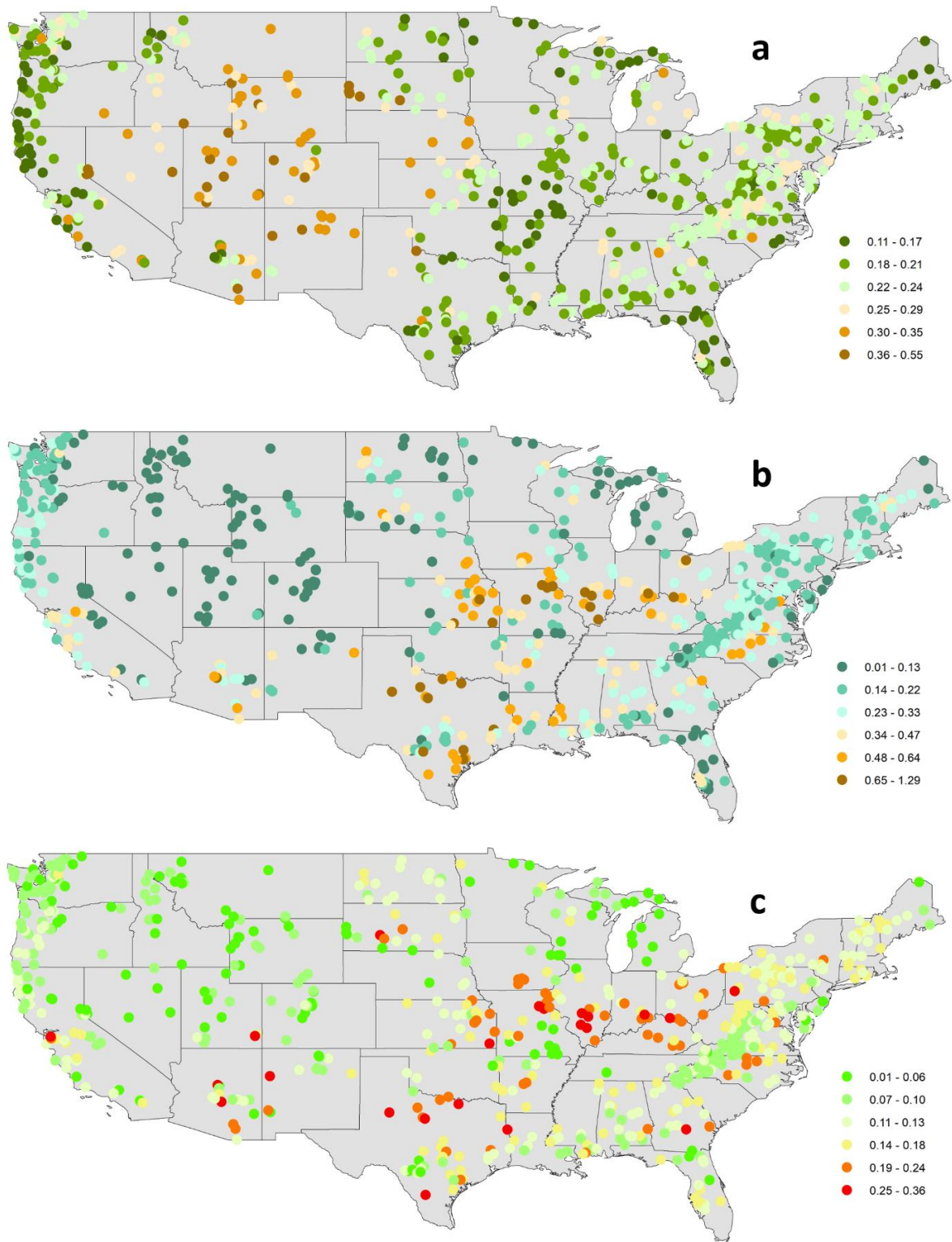
331 **Figure 5.** Spatial maps of streamflow indices associated with a rising limb (a) rising limb density [day^{-1}], (b)
 332 rising limb scale parameter, (c) rising limb shape parameter over the CONUS.

333



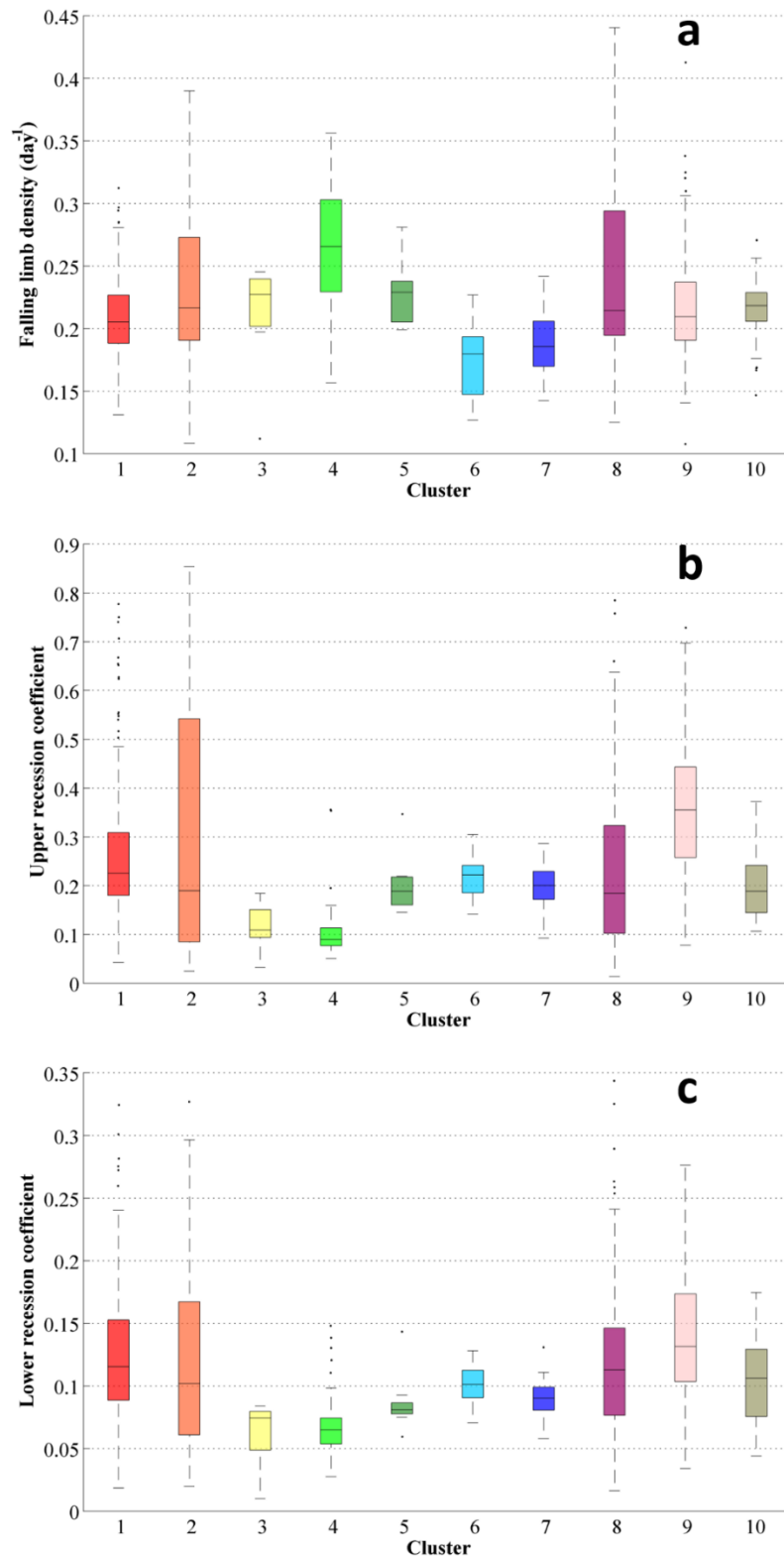
334

335 **Figure 6.** Boxplots of the hydrological descriptors linked with the rising limb (a) rising limb density [day^{-1}], (b)
 336 rising limb scale parameter, (c) rising limb shape parameter of the clusters over the CONUS.



337

338 **Figure 7.** Regional variability of streamflow indices associated with the falling limb (a) falling limb density [day^{-1}], (b) upper recession coefficient, (c) lower recession coefficient over the CONUS.
 339



340

341 **Figure 8.** Boxplots of the streamflow indices related with the falling limb (a) falling limb density [day^{-1}], (b) upper
 342 recession coefficient, (c) lower recession coefficient of the clusters.

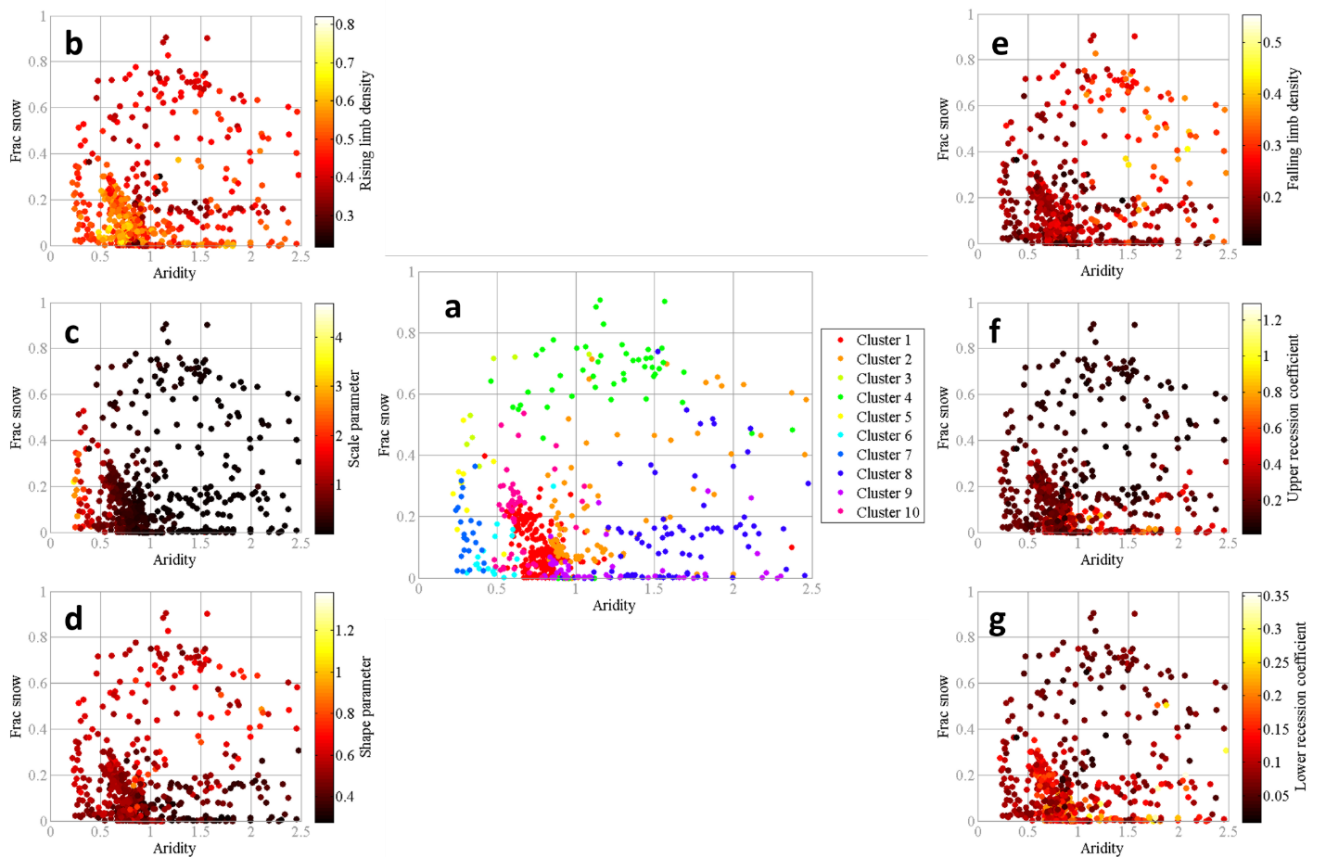
343

344

345 **Table 2** Correlation (r- values) between streamflow indices and the catchment attributes. Green colored
 346 coefficients represent positive correlation, and the red-colored correlation coefficients represent the negative
 347 correlation. Corresponding (*p*- values) are shown in brackets. Insignificant correlations (*p* > 0.05) are marked
 348 yellow.

r- value	Rising limb density	Scale parameter	Shape parameter	Falling limb density	Upper recession coefficient	Lower recession coefficient
Area	-0.30 (0.00)	-0.17 (0.00)	-0.06 (0.11)	-0.13 (0.00)	-0.06 (0.10)	-0.06 (0.11)
Mean elevation	-0.20 (0.00)	-0.13 (0.00)	0.41 (0.00)	0.55 (0.00)	-0.40 (0.00)	-0.35 (0.00)
Mean slope	-0.06 (0.13)	0.35 (0.00)	0.36 (0.00)	0.18 (0.00)	-0.38 (0.00)	-0.37 (0.00)
Precipitation seasonality	-0.04 (0.26)	-0.36 (0.00)	-0.14 (0.00)	0.01 (0.75)	0.17 (0.00)	0.22 (0.00)
Frac of precp as snow	-0.33 (0.00)	-0.04 (0.27)	0.53 (0.00)	0.42 (0.00)	-0.46 (0.00)	-0.39 (0.00)
Aridity	-0.10 (0.01)	-0.53 (0.00)	-0.16 (0.00)	0.39 (0.00)	0.04 (0.30)	0.03 (0.45)
High precp freq	0.08 (0.04)	-0.56 (0.00)	-0.42 (0.00)	0.12 (0.00)	0.31 (0.00)	0.27 (0.00)
High precp dur	-0.15 (0.00)	0.00 (0.97)	-0.07 (0.09)	0.12 (0.00)	-0.11 (0.01)	-0.17 (0.00)
Low precp freq	0.00 (0.91)	-0.63 (0.00)	-0.45 (0.00)	0.17 (0.00)	0.26 (0.00)	0.19 (0.00)
Low precp dur	-0.03 (0.49)	-0.25 (0.00)	-0.29 (0.00)	0.11 (0.00)	0.07 (0.07)	0.01 (0.84)
Depth to bedrock	-0.32 (0.00)	-0.21 (0.00)	-0.16 (0.00)	-0.19 (0.00)	0.19 (0.00)	0.21 (0.00)
Sand frac	-0.28 (0.00)	-0.02 (0.62)	0.37 (0.00)	-0.02 (0.63)	-0.38 (0.00)	-0.23 (0.00)
Clay frac	0.26 (0.00)	-0.15 (0.00)	-0.47 (0.00)	0.00 (0.93)	0.52 (0.00)	0.32 (0.00)
Forest frac	0.10 (0.01)	0.46 (0.00)	0.41 (0.00)	-0.17 (0.00)	-0.31 (0.00)	-0.28 (0.00)
LAI maximum	0.20 (0.00)	0.41 (0.00)	0.17 (0.00)	-0.37 (0.00)	-0.09 (0.03)	-0.04 (0.28)
Green veg frac max	0.18 (0.00)	0.44 (0.00)	0.15 (0.00)	-0.40 (0.00)	-0.05 (0.16)	-0.01 (0.74)
Subsurface porosity	-0.16 (0.00)	-0.06 (0.12)	-0.16 (0.00)	-0.08 (0.03)	0.13 (0.00)	0.16 (0.00)
Subsurface permeability	-0.11 (0.00)	-0.04 (0.34)	0.06 (0.12)	0.03 (0.39)	-0.09 (0.02)	-0.18 (0.00)

349



351

352 **Figure 9.** (a) Comparison of the hydrological clusters of Jehn et al. (2020) with the climate index space (fraction
 353 of precipitation falling as snow vs. aridity). Single dots show the catchments and are colored by their hydrological
 354 clusters. Comparison of the streamflow indices in climate index space (b) rising limb density (c) rising limb scale
 355 parameter, (d) rising limb shape parameter, (e) falling limb density, (f) upper recession coefficient, (g) lower
 356 recession coefficient for all catchments. Single dots show the catchments and are colored according to the value
 357 of the streamflow indices.

358

359 4.2 Influence of Attributes of Climate to Streamflow Indices

360 The climatic indices indicate a more substantial influence on hydrological signatures than the topographic, soil,
 361 land cover, and geological attributes combined (Addor et al., 2018, Stein et al., 2021). Additionally, the findings
 362 of Jehn et al. (2020) highlighted that the climate appears to be the most critical factor influencing hydrological
 363 behavior in the CAMELS dataset as a whole, and depending on the location, either aridity, snow, or seasonality
 364 are most important. Hence, the streamflow indices are then examined in the climate index space (aridity along x-
 365 axis and fraction of precipitation falling as snow along the y-axis) to evaluate the main drivers of the catchments.
 366 Single dots show the catchments and are colored by their hydrological clusters (Fig. 9.a).

367 Clusters 5, 6, 7, 1, 10 are characterized by a low fraction of precipitation falling as snow and humid climate,
 368 whereas Clusters 3, 4 have humid climate experiencing a high fraction of precipitation falling as snow (Fig. 9.a).
 369 Clusters 2, 8, 9 are featured by a low fraction of precipitation falling as snow and arid climate (Fig. 9.a). The three
 370 categories mentioned above are referred to as G1, G2, and G3, respectively.

371 Clusters G1 with a low fraction of precipitation falling as snow with humid climate show (Clusters 1, 9, 10) high
372 rising limb densities (Fig. 9.b) and (Clusters 5, 7) high rising limb scale parameters (Fig. 9.c). This is because the
373 rising limb density negatively correlates with fraction of precipitation falling as snow (Table 2: $r = -0.33$, Fig.
374 9.b), whereas the rising limb scale parameter negatively correlates with aridity (Table 2: $r = -0.53$, Fig. 9.c).
375 Moreover, these Clusters G1 experience a low value of (Clusters 6, 7) falling limb density (Fig. 9.e). This is
376 because the falling limb density positively correlates with the climate indices (Table 2: $r = 0.42$ for fraction of
377 precipitation falling as snow and $r = 0.39$ for aridity, Fig. 9.e).

378 As mentioned earlier, Clusters G2 with humid climate and with a high fraction of precipitation falling as snow
379 (Clusters 3, 4) display low values of rising limb density as rising limb density correlates negatively with the
380 fraction of precipitation falling as snow (Table 2: $r = -0.33$, Fig. 9.b). G2 witnesses higher values of rising limb
381 shape parameter due to its negative correlation with aridity ($r = -0.16$) and positive correlation with the fraction
382 of precipitation falling as snow (Table 2: $r = 0.53$, Fig. 9.d). Furthermore, the Clusters of G2 (Clusters 3, 4) show
383 low values of recession coefficients as they depict a strong negative correlation with the fraction of precipitation
384 falling as snow (Table 2: upper_r = -0.46, and lower_r = -0.39, Fig. 9.f, g).

385 Low values of rising limb scale and shape parameters are noticed for the Clusters 2, 9, 8 (Clusters G3) with arid
386 climate and low fraction of precipitation falling as snow (Fig. 9.c, d) due to its negative correlation with aridity as
387 stated earlier. Cluster 8 experiences the maximum values of falling limb density (Fig. 9.e) where the region
388 witnesses low fraction of snow and arid catchments, due to its strong positive correlates with the aridity ($r = 0.39$).

389 **5 Concluding remarks**

390 Streamflow hydrograph portrays the time distribution of runoff at the point of measurement by a single curve, and
391 the hydrographs are characterized by their time irreversibility property. In this study, the indices related to this
392 characteristic feature are used to study the catchment drivers of streamflow hydrograph. The streamflow indices
393 associated with the time irreversibility of hydrograph open new opportunities to investigate the interaction
394 between topography, soil, climate, vegetation, geology that drive the hydrological behavior of catchments.
395 Moreover, most of the previously presented hydrologic indices are employed only for time-symmetric processes
396 (McMillan, 2021); the importance of the time irreversibility of streamflow is highlighted in this study. The indices
397 associated with rising and falling limbs are primarily correlated to distinct catchment attributes, establishing a
398 relationship between the indices and catchment attributes such as climate, topography, soil, geology, and
399 vegetation to delineate the controlling drivers in corresponding hydrograph sections. A set of streamflow indices
400 with temporal asymmetry for 671 catchments in the United States is presented in this study. The regional
401 variations among catchments over the United States are compared and discussed using the spatial maps of
402 streamflow indices. Such spatial maps of the streamflow indices supplement the hydrometeorological time series
403 and catchment attributes provided by Addor et al. (2017).

404 The study showed that the rising limb density is mainly governed by the elevation and fraction of precipitation
405 falling as snow. Climate indices, mean elevation, and the fraction of precipitation falling as snow mainly influence
406 falling limb density. In contrast, the aridity and frequency of precipitation drive the rising limb scale parameter.
407 Furthermore, forest fraction, the fraction of precipitation falling as snow, mean slope, mean elevation, sand
408 fraction, and precipitation frequency influence the rising limb shape parameter. Mean elevation, mean slope, clay,

409 the fraction of precipitation falling as snow, forest fraction, and sand fraction all determine recession coefficients.
410 Finally, streamflow indices are studied in the climate index space to isolate the runoff generation's leading drivers.
411 High rising limb densities and rising limb scale parameters are observed in catchments with low precipitation
412 falling as snow and a humid climate. It is observed that the catchments with a humid climate and a high fraction
413 of precipitation falling as snow display low values of rising limb density, high values of the rising limb shape
414 parameter, and low values of recession coefficients. The lowest values of rising limb scale and shape parameters,
415 and the highest values of falling limb density, are seen in catchments of arid climates and a low fraction of
416 precipitation falling as snow.

417 In general, the contribution of this work lies in differentiating hydrographs depending on their time irreversibility
418 property and using the corresponding indices to provide an alternative methodology for identifying the drivers of
419 streamflow hydrographs. In the context of large sample hydrology research, the concept of time-irreversibility
420 and the indices associated with it could also be used to describe the drivers at catchment scale. It must be noted
421 that each attribute (e.g., climate vegetation, soil, geology) usually does not exist independently in space but is
422 closely interwoven, resulting in various strongly correlated attributes in a catchment (Jehn et al., 2020; Stein et
423 al., 2021). However, it would be beyond the scope of this paper to describe all probable relationships between
424 attributes. Keeping this in mind, the main focus of this study was constrained to only identify the controlling
425 attributes of streamflow indices. Another limitation of the work is related with the characterization of recessions
426 used. Future work may investigate using the inflection point or another recession separation technique to
427 characterize recessions.

428

429 *Data availability.* The CAMELS dataset can be found at <https://doi.org/10.5194/hess21-5293-2017> (Addor et al.
430 2017). The hydrometeorological time series (<https://doi.org/10.5065/D6MW2F4D>) used in this paper are freely
431 available online.

432 *Competing interests.* The authors declare that they have no conflict of interest.

433 *Acknowledgements.* We would like to thank all the people who created the CAMELS dataset. We sincerely thank
434 Editor Elena Toth, Dr. Wouter Knoben, and the anonymous reviewer for patiently reviewing the manuscript and
435 offering valuable critical comments to improve the manuscript. Their suggestions have significantly improved the
436 quality of our contribution to this revised manuscript.

437 The funding received from the Ministry of Earth Sciences (MoES), Government of India, through the project,
438 “Advanced Research in Hydrology and Knowledge Dissemination”, Project No.: MOES/PAMC/H&C/41/2013-
439 PC-II, is gratefully acknowledged.

440

441 **References**

442

443 Addor, Newman, A. J., Mizukami, N. and Clark, M. P.: The CAMELS data set: catchment attributes and
444 meteorology for large-sample studies, *Hydrol. Earth Syst. Sci.*, 21(10), 5293–5313, doi:10.5194/hess-21-5293-
445 2017, 2017.

446 Addor, Nearing, G., Prieto, C., Newman, A. J., Le Vine, N. and Clark, M. P.: A Ranking of Hydrological

447 Signatures Based on Their Predictability in Space, *Water Resour. Res.*, 54(11), 8792–8812,
448 doi:10.1029/2018WR022606, 2018.

449 Addor, N., Do, H. X., Alvarez-Garreton, C., Coxon, G., Fowler, K. and Mendoza, P. A.: Large-sample hydrology:
450 recent progress, guidelines for new datasets and grand challenges, *Hydrol. Sci. J.*, 65(5), 712–725,
451 doi:10.1080/02626667.2019.1683182, 2020.

452 Alvarez-Garreton, C., Mendoza, P. A., Pablo Boisier, J., Addor, N., Galleguillos, M., Zambrano-Bigiarini, M.,
453 Lara, A., Puelma, C., Cortes, G., Garreaud, R., McPhee, J. and Ayala, A.: The CAMELS-CL dataset: Catchment
454 attributes and meteorology for large sample studies-Chile dataset, *Hydrol. Earth Syst. Sci.*, 22(11), 5817–5846,
455 doi:10.5194/hess-22-5817-2018, 2018a.

456 Alvarez-Garreton, C., Mendoza, P. A., Boisier, J. P., Addor, N., Galleguillos, M., Zambrano-Bigiarini, M., Lara,
457 A., Puelma, C., Cortes, G., Garreaud, R., McPhee, J. and Ayala, A.: The CAMELS-CL dataset: catchment
458 attributes and meteorology for large sample studies – Chile dataset, *Hydrol. Earth Syst. Sci.*, 22(11), 5817–5846,
459 doi:10.5194/hess-22-5817-2018, 2018b.

460 Arsenault, R., Bazile, R., Ouellet Dallaire, C. and Brissette, F.: CANOPEX: A Canadian hydrometeorological
461 watershed database, *Hydrol. Process.*, 30(15), 2734–2736, doi:10.1002/hyp.10880, 2016.

462 Berghuijs, W. R., Sivapalan, M., Woods, R. A. and Savenije, H. H. G.: Patterns of similarity of seasonal water
463 balances: A window into streamflow variability over a range of time scales, *Water Resour. Res.*, 50(7), 5638–
464 5661, doi:10.1002/2014WR015692, 2014.

465 Blöschl, G., Hall, J., Viglione, A., Perdigão, R. A. P., Parajka, J., Merz, B., Lun, D., Arheimer, B., Aronica, G.
466 T., Bilibashi, A., Boháč, M., Bonacci, O., Borga, M., Čanjevac, I., Castellarin, A., Chirico, G. B., Claps, P.,
467 Frolova, N., Ganora, D., Gorbachova, L., Gül, A., Hannaford, J., Harrigan, S., Kireeva, M., Kiss, A., Kjeldsen, T.
468 R., Kohnová, S., Koskela, J. J., Ledvinka, O., Macdonald, N., Mavrova-Guirguinova, M., Mediero, L., Merz, R.,
469 Molnar, P., Montanari, A., Murphy, C., Osuch, M., Ovcharuk, V., Radevski, I., Salinas, J. L., Sauquet, E., Šraj,
470 M., Szolgay, J., Volpi, E., Wilson, D., Zaimi, K. and Živković, N.: Changing climate both increases and decreases
471 European river floods, *Nature*, 573(7772), 108–111, doi:10.1038/s41586-019-1495-6, 2019.

472 Clark, M. P., McMillan, H. K., Collins, D. B. G., Kavetski, D. and Woods, R. A.: Hydrological field data from a
473 modeller’s perspective: Part 2: Process-based evaluation of model hypotheses, *Hydrol. Process.*, 25(4), 523–543,
474 doi:10.1002/hyp.7902, 2011.

475 Coxon, G., Freer, J., Wagener, T., Odoni, N. A. and Clark, M.: Diagnostic evaluation of multiple hypotheses of
476 hydrological behaviour in a limits-of-acceptability framework for 24 UK catchments, *Hydrol. Process.*, 28(25),
477 6135–6150, doi:10.1002/hyp.10096, 2014.

478 Coxon, G., Addor, N., Bloomfield, J. P., Freer, J., Fry, M., Hannaford, J., Howden, N. J. K., Lane, R., Lewis, M.,
479 Robinson, E. L., Wagener, T. and Woods, R.: CAMELS-GB: hydrometeorological time series and landscape
480 attributes for 671 catchments in Great Britain, *Earth Syst. Sci. Data*, 12(4), 2459–2483, doi:10.5194/essd-12-
481 2459-2020, 2020.

482 Do, H. X., Gudmundsson, L., Leonard, M. and Westra, S.: The Global Streamflow Indices and Metadata Archive
483 (GSIM) – Part 1: The production of a daily streamflow archive and metadata, *Earth Syst. Sci. Data*, 10(2), 765–
484 785, doi:10.5194/essd-10-765-2018, 2018.

485 Duan, Q., Schaake, J., Andréassian, V., Franks, S., Goteti, G., Gupta, H. V., Gusev, Y. M., Habets, F., Hall, A.,
486 Hay, L., Hogue, T., Huang, M., Leavesley, G., Liang, X., Nasonova, O. N., Noilhan, J., Oudin, L., Sorooshian,
487 S., Wagener, T. and Wood, E. F.: Model Parameter Estimation Experiment (MOPEX): An overview of science
488 strategy and major results from the second and third workshops, *J. Hydrol.*, 320(1–2), 3–17,
489 doi:10.1016/j.jhydrol.2005.07.031, 2006.

490 Ehret, U., Gupta, H. V., Sivapalan, M., Weijs, S. V., Schymanski, S. J., Blöschl, G., Gelfan, A. N., Harman, C.,
491 Kleidon, A., Bogaard, T. A., Wang, D., Wagener, T., Scherer, U., Zehe, E., Bierkens, M. F. P., Di Baldassarre,
492 G., Parajka, J., van Beek, L. P. H., van Griensven, A., Westhoff, M. C. and Winsemius, H. C.: Advancing
493 catchment hydrology to deal with predictions under change, *Hydrol. Earth Syst. Sci.*, 18(2), 649–671,
494 doi:10.5194/hess-18-649-2014, 2014.

495 Ghiggi, G., Humphrey, V., Seneviratne, S. I. and Gudmundsson, L.: GRUN: an observation-based global gridded
496 runoff dataset from 1902 to 2014, *Earth Syst. Sci. Data*, 11(4), 1655–1674, doi:10.5194/essd-11-1655-2019, 2019.

497 Gudmundsson, L., Do, H. X., Leonard, M. and Westra, S.: The Global Streamflow Indices and Metadata Archive
498 (GSIM) – Part 2: Quality control, time-series indices and homogeneity assessment, *Earth Syst. Sci. Data*, 10(2),
499 787–804, doi:10.5194/essd-10-787-2018, 2018.

500 Gupta, H. V., Perrin, C., Blöschl, G., Montanari, A., Kumar, R., Clark, M. and Andréassian, V.: Large-sample
501 hydrology: a need to balance depth with breadth, *Hydrol. Earth Syst. Sci.*, 18(2), 463–477, doi:10.5194/hess-18-
502 463-2014, 2014.

503 Jehn, F. U., Bestian, K., Breuer, L., Kraft, P. and Houska, T.: Using hydrological and climatic catchment clusters
504 to explore drivers of catchment behavior, *Hydrol. Earth Syst. Sci.*, 24(3), 1081–1100, doi:10.5194/hess-24-1081-
505 2020, 2020.

506 Khrystyuk, B., Gorbachova, L. and Koshkina, O.: The impact of climatic conditions of spring flood formation
507 on hydrograph shape of the Desna River, *Meteorol. Hydrol. Water Manag.*, 5(1), 63–70,
508 doi:10.26491/mhwm/67914, 2017.

509 Knoben, W. J. M., Woods, R. A. and Freer, J. E.: A Quantitative Hydrological Climate Classification Evaluated
510 With Independent Streamflow Data, *Water Resour. Res.*, 54(7), 5088–5109, doi:10.1029/2018WR022913,
511 2018.

512 Koutsoyiannis, D.: Simple stochastic simulation of time irreversible and reversible processes, *Hydrol. Sci. J.*,
513 doi:10.1080/02626667.2019.1705302, 2020.

514 Kuentz, A., Arheimer, B., Hundecha, Y. and Wagener, T.: Understanding hydrologic variability across Europe
515 through catchment classification, *Hydrol. Earth Syst. Sci.*, 21(6), 2863–2879, doi:10.5194/hess-21-2863-2017,
516 2017.

517 Linke, S., Lehner, B., Ouellet Dallaire, C., Ariwi, J., Grill, G., Anand, M., Beames, P., Burchard-Levine, V.,
518 Maxwell, S., Moidu, H., Tan, F. and Thieme, M.: Global hydro-environmental sub-basin and river reach
519 characteristics at high spatial resolution, *Sci. Data*, 6(1), 283, doi:10.1038/s41597-019-0300-6, 2019.

520 Mathai and Mujumdar, P. P.: Multisite Daily Streamflow Simulation With Time Irreversibility, *Water Resour.*
521 *Res.*, 55(11), 9334–9350, doi:10.1029/2019WR025058, 2019.

522 McMillan, H. K.: A review of hydrologic signatures and their applications, *WIREs Water*, 8(1), 1–23,
523 doi:10.1002/wat2.1499, 2021.

524 McMillan, H. K., Clark, M. P., Bowden, W. B., Duncan, M. and Woods, R. A.: Hydrological field data from a
525 modeller’s perspective: Part 1. Diagnostic tests for model structure, *Hydrol. Process.*, 25(4), 511–522,
526 doi:10.1002/hyp.7841, 2011.

527 Newman, A. J., Clark, M. P., Sampson, K., Wood, A., Hay, L. E., Bock, A., Viger, R. J., Blodgett, D., Brekke,
528 L., Arnold, J. R., Hopson, T. and Duan, Q.: Development of a large-sample watershed-scale hydrometeorological
529 data set for the contiguous USA: data set characteristics and assessment of regional variability in hydrologic model
530 performance, *Hydrol. Earth Syst. Sci.*, 19(1), 209–223, doi:10.5194/hess-19-209-2015, 2015.

531 Richter, B. D., Baumgartner, J. V., Powell, J. and Braun, D. P.: A Method for Assessing Hydrologic Alteration
532 within Ecosystems, *Conserv. Biol.*, 10(4), 1163–1174, doi:10.1046/j.1523-1739.1996.10041163.x, 1996.

533 Roberts, M. C. and Klingeman, P. C.: The influence of landform and precipitation parameters on flood
534 hydrographs, *J. Hydrol.*, 11(4), 393–411, doi:10.1016/0022-1694(70)90004-1, 1970.

535 Rogers, W. F.: New concept in hydrograph analysis, *Water Resour. Res.*, 8(4), 973–981,
536 doi:10.1029/WR008i004p00973, 1972.

537 Sawicz, K., Wagener, T., Sivapalan, M., Troch, P. A. and Carrillo, G.: Catchment classification : empirical
538 analysis of hydrologic similarity based on catchment function in the eastern USA, *Hydrol. Earth Syst. Sci.*, 8(3),
539 2895–2911, doi:10.5194/hess-15-2895-2011, 2011.

540 Sawicz, K. A., Kelleher, C., Wagener, T., Troch, P., Sivapalan, M. and Carrillo, G.: Characterizing hydrologic
541 change through catchment classification, *Hydrol. Earth Syst. Sci.*, 18(1), 273–285, doi:10.5194/hess-18-273-
542 2014, 2014.

543 Serinaldi, F. and Kilsby, C. G.: Irreversibility and complex network behavior of stream flow fluctuations, *Phys.*
544 *A Stat. Mech. its Appl.*, 450, 585–600, doi:10.1016/j.physa.2016.01.043, 2016.

545 Shamir, E., Imam, B., Morin, E., Gupta, H. V. and Sorooshian, S.: The role of hydrograph indices in parameter
546 estimation of rainfall-runoff models, *Hydrol. Process.*, 19(11), 2187–2207, doi:10.1002/hyp.5676, 2005.

547 Singh, V. P.: Effect of spatial and temporal variability in rainfall and watershed characteristics on stream flow
548 hydrograph, *Hydrol. Process.*, 11(12), 1649–1669, doi:10.1002/(SICI)1099-1085(19971015)11:12<1649::AID-
549 HYP495>3.0.CO;2-1, 1997.

550 Stagge, J. H. and Moglen, G. E.: A nonparametric stochastic method for generating daily climate-adjusted
551 streamflows, *Water Resour. Res.*, 49, 6179–6193, doi:10.1002/wrcr.20448, 2013.

552 Stein, L., Clark, M. P., Knoben, W. J. M., Pianosi, F. and Woods, R. A.: How Do Climate and Catchment
553 Attributes Influence Flood Generating Processes? A Large-Sample Study for 671 Catchments Across the
554 Contiguous USA, *Water Resour. Res.*, 57(4), 1–21, doi:10.1029/2020WR028300, 2021.

555 Szilagyi, J., Balint, G. and Csik, A.: Hybrid, Markov chain-based model for daily streamflow generation at
556 multiple catchment sites, *J. Hydrol. Eng.*, 11(3), 245–256, 2006.